Proceedings of ICFDP9:
Ninth International Congress of Fluid Dynamics & Propulsion
December 18-21, 2008, Alexandria, Egypt

ICFDP9-EG-220

UNSTEADY VORTICITY FIELDS IN A LONG NARROW CHANNEL WITH ENDWALL DISTURBANCES AND SIDEWALL INJECTION

Abdelkarim Hegab*[a], Mostafa Nasr[b],

[a] *Ass. Prof. Menoufia Universit, Faculty of Engineering, Shebin Elkom, Menoufia, EGYPT*
[b] *Ass. Prof. Menoufia Universit, Faculty of Engineering, Shebin Elkom, Menoufia, EGYPT*

**Corresponding author:* hegab2002us@yahoo.com, Tel.: +2-048-2237840, Fax: +2-048-2235695

ABSTRACT

In this paper, analytical, computational, and experimental studies are employed to describe the generation and propagation of intense unsteady vorticity in a long, narrow chamber with end wall disturbances and steady sidewall mass injection. This mechanism mimics the unsteady burning processes in real solid rocket motor chamber at resonance and non-resonance frequencies. The analytical approach is based on the reduced form of the Navier-Stokes using asymptotic technique. The equations that arises from the analysis posses wave properties and are solved in an initial value sense. Experimental test rig is carried out on a chamber closed at the head end and opened at the exit end. The acoustic waves are generated at the head end by an oscillating piston whose frequencies away from, near to or at the resonance ones. The pressure histories are recorded using capacitance pressure transducers connected with a computer has data acquisition card built in through Lab-view software. The pressure traces are recorded at different axial locations along the chamber. The results show that unexpectedly large transient shear stresses are created at the sidewall of the chamber and convected downstream by the bulk motion of the internal flow. These stresses may cause scouring effect and large transient heat transfer on the combustion surface. A comparison between the analytical, computational and experimental results is performed

KEYWORDS:

Permeable Walls, Solid Rocket Motor Chamber, Unsteady Vorticity, Mass Injection, Endwall disturbances

INTRODUCTION

In the present paper analytical, computational, and experimental studies are performed to describe the nature of a low Mach number and weakly viscous flow field generated in a long, narrow chamber with steady sidewall mass injection and end wall disturbances. The inviscid rotational steady injected flow interacts with the irrotational acoustic field to generate unsteady vorticity at the sidewall and is penetrated toward the centerline by the steady transverse velocity component. The axially distributed transverse velocity on the sidewall is a prescribed and the temperature of the injected gas is specified.

The propagation of acoustic waves (irrotational field only) in closed or open end tubes without any consideration for the mass injection from the sidewall have been studied intensively by the experimental and theoretical approaches, [1-10]. These studies described the behavior of finite amplitude waves at or near resonance frequencies and the effect of nonlinearity on the waveform. Erickson et al. [1] studied theoretically the behavior of forced finite amplitude oscillations in cylindrical constant and variable area ducts whose ends are closed. Shock waves are observed in the form of saw-tooth like waveforms in the case of constant area duct when the duct oscillates at resonance frequency. Similar theoretical and experimental works are carried out by Zapirov and Ilhamov [2]. Merkli and Thomann [3] studied experimentally the thermo-acoustic effects in resonant closed tube. Their results showed the steepness of the wave and the shock wave formation near or at the resonance frequencies.

Wang and Kassoy [4] also studied the nonlinear oscillations in a resonance gas column. They studied both closed and open tubes. In case of closed tube, shock wave appears with small limiting amplitude as a result of nonlinearity. While in case of open end the shock wave appears intermittently. This conclusion is also drawn by Jimeniz, [5]. The effect of convergent-divergent nozzle appended a constant area duct on the behavior of the traveling acoustic waves is described theoretically by Sileem [6] and Experimentally by

Sileem and Nasr [7]. For duct ended with convergent –area portion, the wave steepness increase and N-type waveform is noticed. While for duct ended with convergent-divergent area type, the wave amplitude near the end of the constant portion duct is greater than that of convergent-part only. Seymour and Mortell [8] studied the acoustic wave damping from full opened, partially opened, and full closed gas column. The described the wave pattern at resonance conditions. For full opened tube, the wave damping was related to the energy radiation into the adjacent medium. In case of closed end tubes, no energy radiated outside of the tube and in turn shock wave is formed. In case of partially opened end tube, part of acoustic energy is radiated which prevent shock wave formation. Similar experimental and theoretical studies have been carried by Disselhorst and Wijngarden [9], and Garcia and Linan [10].

The interaction between the propagation of acoustic waves in closed or open end tubes with the mass injection from the sidewall have been studied [11-13]. Staab et al. [11], Rempe et al. [12] and Zhao et al. [13] employ asymptotic methods to demonstrate that unsteady addition of mass from the lateral boundaries of a cylinder is the immediate source of acoustic disturbances that propagate in the low axial Mach number (M), high Reynolds number (Re) mean flow. Their analytical results are used to prove that an inviscid and non-conducting interaction between the acoustic transients and the fluid injected from the sidewall causes transverse axial velocity gradients (vorticity) and transverse temperature gradients (heat transfer) to appear on the sidewalls. Subsequently, the transverse velocity field driven by the prescribed wall injection convects the gradients into the interior of the flow. The analyses show that the nondimensional acoustic axial velocity is O(1) and the temperature disturbance is O(M) for M<<1. In contrast, the transverse velocity gradient is O(1/M) and the transverse temperature gradient is O(1), each one order larger than the relevant disturbance itself. This difference is attributable to the interaction phenomena cited above which occurs on a short radial length scale, O(MR'), where R' is the radius of the cylinder.

In general, velocity and vorticity dynamics were emphasized for several reasons. First, several researches have been focused entirely on the evolution of assumed irrotational (acoustic) velocity and pressure disturbances, to the exclusion of rotational flow (vorticity) transients. Secondly, several investigators developed a competitive linear theory to demonstrate that accurate descriptions of internal flow dynamics frequently require the presence of co-existing rotational and irrotational velocity fields (see for example, Flandro [14], Majdalani and Van Moorhem [15). Finally, systematic nonlinear asymptotic modeling, valid for larger amplitude disturbances, shows formally that the basic velocity and pressure fields are decoupled from thermal processes (see for example, Staab et al.[11] , Zhao et al. [13]). It follows that velocity and vorticity dynamics can be assessed without concern for temperature effects.

Vuillot and Avalon [16] predicted the presence of vorticity in an injected internal flow using a computational solution to the Navier Stokes equation. Similar results were obtained by Smith et al. [17] in both cases the acoustic disturbances are generated by imposed pressure variations along an axial location. Related numerical calculations have been carried out by Tseng et al. [18] and Roh and Yang [19] to include the effect of exothermic combustion reactions adjacent to the sidewall. The temperature variations observed in these studies arise from flame zone effects, rather than the acoustic disturbance-injected fluid interaction mentioned previously.

Recently, Hegab [20] and Hegab et al. [21] studied analytically and computationally the internal flow temperature and vorticity dynamics in channel with transient mass addition. Experimental observation by Vetel et al. [22,23] supported the concepts of vorticity generation featured by Hegab and coworkers.

In the present paper, the inviscid rotational steady injected flow interacts with the transient end wall velocity to generate unsteady vorticity at the sidewall and is penetrated toward the centerline by the steady transverse velocity component. Results are given for a nondimensional sidewall injection distribution composed of a steady spatially uniform part and a similar amplitude oscillatory part that is axially distributed. The amplitude of the latter is large enough to ensure that fully nonlinear fluid dynamics is evolving in the flow field (Staab et al [11]). The results of the present study show that surprisingly large transient vorticity are present on the sidewalls and in the interior of the channel, even when the transverse fluid injection is isothermal. This unexpected phenomenon arises from an interesting interaction between acoustic disturbances present in the low Mach number internal flow and the fluid injected from the boundary.

Comparisons of time-evolution of velocity and pressure distributions for non-resonant and near resonant oscillation frequencies are used to show how relatively large amplitude disturbances evolve in the chamber.

The Physical and Mathematical Formulation:-

The main objective of the current work is to model the flow in a chamber with a time-dependent injection velocity with the goal of understanding the heat transfer and temperature dynamics that accompany the vorticity generation across the entire chamber. The flow occurs in a planar chamber geometry of length $L^{'}$ (primes denote dimensional variables), chamber-half height $H^{'}$, and an aspect ratio ($\delta = L^{'}/H^{'}$) with an imposed pressure node at the exit and an impermeable wall at the head end. Inert gas, injected through the porous side walls with a characteristic velocity $V^{'}_{yo}$, induces an axial flow characterized by $U^{'}_{zo} = \delta V^{'}_{yo}$ to mimic the evolution of combustion products from solid propellant burning, $r_b(x,t)$. Where $v'_{rws}(x)$ are the *steady* injection velocity

components respectively. $p_o^{'}$ is representative of the exit pressure from the chamber and $T_o^{'}$ is the temperature of the fluid injected from the side-wall.

The mathematical model is based on the following non-dimensional conservation form of the unsteady, compressible, 2-D, parabolized Navier-Stokes equations describing both fluid dynamics and acoustics in a perfect gas in general curvilinear coordinates;

$$\frac{\partial Q}{\partial t}+\frac{\partial E}{\partial x}+\frac{\partial F}{\partial y}=0, \qquad (1)$$

where; $Q=\begin{bmatrix}\rho\\ \rho u-\\ \rho v-\\ E_T-\end{bmatrix}$, $E=\begin{bmatrix}M\,\rho u\\ M\,\rho u^2+\dfrac{1}{\gamma M^2}p\\ M\,\rho uv-\\ M\{E_T+(\gamma-1)p\}u-\end{bmatrix}$,

$$F=\begin{bmatrix}M\,\rho v\\ M\,\rho uv-\dfrac{\delta^2 M}{R_e}u_y\\ M\,\rho v^2+\dfrac{\delta^2}{\gamma M}p\\ M\{E_T+(\gamma-1)p\}v-\dfrac{\gamma\delta^2 M}{R_e P_r}T_y\end{bmatrix}$$

E_T is the total energy ($\rho[T+\gamma(\gamma-1)M^2(u^2+(v/\delta)^2]$) and the equation of state for a perfect gas is;

$$p=\rho T \qquad (2)$$

It is assumed that the specific heats, the viscosity and conductivity coefficients are constant. Non-dimensional variables defined in terms of dimensional quantities denoted by a prime, are given by;

$$p=p^{'}/p_o^{'},\ \rho=\rho^{'}/\rho_o^{'},\ T=T^{'}/T_o^{'},\quad u=u^{'}/U_{z_o}^{'},\ v=v^{'}/\left(U_{z_o}^{'}/\delta\right),$$
$$x=x^{'}/L^{'},\ y=y^{'}/H^{'},\ t=t^{'}/t_a^{'} \qquad (3)$$

Characteristic length scales for the axial and transverse variables are chosen to be duct length $L^{`}$ and the height $H^{'}$, respectively. Time is non-dimensionalized with respect to the axial acoustic time $t_a^{'}=L^{'}/C_o^{'}$. The characteristic axial flow Mach number, Prandtl number, flow and acoustic Reynolds numbers are defined respectively as follows;

$$M=\frac{U_{z_o}^{'}}{C_o^{'}},\quad P_r=\frac{\mu_o^{'}C_{p_o}^{'}}{k_o^{'}},\quad R_e=\frac{\rho_o^{'}U_{z_o}^{'}L^{'}}{\mu_o^{'}},\ and\ R_{e_A}=\frac{R_e}{M} \qquad (4)$$

Parameters ranges of interest include M≤ $O(10^{-1})$ and $R_e=O(10^5\text{-}10^6)$

2.1 The Initial and Boundary Conditions

The solutions to (1) and (2) must satisfy boundary conditions on the endwall (x=0), the sidewall (y=1), the centerline (y=0) and the exit plane x=1 of the chamber. For t≤0, a steady internal flow is generating by an axial variation, time-independent side wall transverse velocity with $V\big|_{wall}=-V_{rws}(x)$, while for t>0, an end wall disturbances is initiated at the head end by a moving piston $u\big|_{x=0}=\varepsilon\sin(\omega t)$ for resonance and non-resonance solution. Where ε is the amplitude of the generated acoustic waves. The boundary conditions for the steady and unsteady flows can be written as follows;

x=0; $u\big|_{x=0}=\varepsilon\sin(\omega t)$, v = 0. (5)

x=1; p = 1, "pressure node" (6)

y=0; $v=0,\ \dfrac{\partial u}{\partial y}=\dfrac{\partial T}{\partial y}=\dfrac{\partial p}{\partial y}=\dfrac{\partial \rho}{\partial y}=0$, (7)

y=1; u=0, T=1, and $v=-v_{rws}(x)$ (8)

The initial condition for the steady state flow is given by;

t=0; u=v=0, p=T=1 (9)

and the derived steady state velocity profiles are used as initial conditions for the unsteady flow computations.

2.2 The Analytical Approach

2.2.1 Steady flow

Staab et al. [11] have explained that the complete computed axial velocity field can be divided into a steady parts and unsteady parts as follows;

$$(u,v,P,\rho,T)=(u_s,v_s,P_s,\rho_s,T_s)+\left(\hat{u},\hat{v},\hat{P},\hat{\rho},\hat{T}\right) \qquad (10)$$

where the first terms on the RHS represent the steady flow and the second terms refer to the unsteady components. The steady state flow variables are expanded as;

$$\begin{aligned}&(u_s,v_s)\ \square\ (u_{os},v_{os})+O(M),\\ &(P_s,\rho_s,T_s)\ \square\ 1+M^2(P_{os},\rho_{os},T_{os})+O\left(M^3\right)\end{aligned} \qquad (11)$$

Inserting the expanded flow variables in (11) into the original system of equations (1), Zhao et.al. [13], Hegab [20], and Hegab et al. [21] found the solution for the steady flow variables with axial variation injection velocity for the limit $M\to 0$ and $\delta^2/R_e\to 0$.

2.2.2 Unsteady flow for the irrotational planar component

A steady state flow driven by constant isothermal sidewall injection is computed initially and then used as initial conditions for the unsteady flow analysis. The initial conditions

for the unsteady flow variables $\left(\hat{u},\hat{v},\hat{P},\hat{\rho},\hat{T}\right)$ are zeros and the asymptotic expansions for the velocity components and the thermodynamic variables in the limit M→0 are;

$$u(x,y,t)\sim u_{os}(x,y)+\sum_{n=0}^{\infty}M^{n}\hat{u}_{n}(x,y,t),$$
$$v(x,y,t)\sim v_{os}(x,y)+\sum_{n=0}^{\infty}M^{n}\hat{v}_{n}(x,y,t), \quad (12)$$
$$P(x,y,t)\sim P_{os}(x,y)+\sum_{n=0}^{\infty}M^{n+1}\hat{P}_{n}(x,y,t),$$
$$T(x,y,t)\sim T_{os}(x,y)+\sum_{n=0}^{\infty}M^{n+1}\hat{T}_{n}(x,y,t), \quad (13)$$
$$\rho(x,y,t)=P(x,y,t)/T(x,y,t), \quad \hat{P}_{o}=\hat{\rho}_{o}+\hat{T}_{o}$$

where the subscripts ($_{os}$) refer to the computed steady state flow and the superscript (^) represent the flow variable perturbations. Inserting the expanded flow variables in Eqns.(12) and (13) in Eqn.(1), and gathering the O(M) terms, the weakly rotational equations are deduced and solved together. After straight forward derivation with little bit complexity, the resultant planar acoustic equation can be written as follows;

$$\frac{\partial^{2}\tilde{u_{0}}}{\partial t^{2}}=\frac{\partial^{2}\tilde{u_{0}}}{\partial x^{2}} \quad (14)$$

The suitable boundary conditions for the weakly rotational equation are found by matching equations (12) and (13) with the global boundary conditions in equations (5)-(8). The initial and boundary equations are shown in figure (1) as follows;

$$t=0,\quad \tilde{u_{0}}=0,\quad \frac{\partial\tilde{u_{0}}}{\partial t}=0 \quad (15)$$
$$x=0,\quad \tilde{u_{0}}=\varepsilon\sin\omega t, \quad (16)$$
$$x=1,\quad \frac{\partial\tilde{u_{o}}}{\partial x}=0 \quad (17)$$

Since the left boundary conditions in (16) are nonhomogeneous, the following transformation equation $u=\tilde{u_{0}}-\varepsilon\sin\omega t$ is used to generate homogeneous boundary conditions with a solvable nonhomogeneous wave equation as;

$$\frac{\partial^{2}u}{\partial t^{2}}=\frac{\partial^{2}u}{\partial x^{2}}-\varepsilon\omega^{2}\sin\omega t \quad (18)$$

with the new initial and boundary conditions

$$t=0,\quad u=0,\quad \frac{\partial u}{\partial t}=-\varepsilon\omega \quad (19)$$
$$x=0,\quad u=0 \quad (20)$$
$$x=1,\quad \frac{\partial u}{\partial x}=0 \quad (21)$$

Assume the homogeneous solution for equation (21) is represented by u`(x,t) and keeping the boundary conditions from (19)-(21) as the same for u`(x,t). Using the separation of variable technique, the derived general homogeneous solution can be written as;

$$u`(x,t)=\sum_{n=0}^{n=\infty}\left\{C_{n}\sin\lambda_{n}t+D_{n}\cos\lambda_{n}t\right\}\sin\lambda_{n}x \quad (22)$$

where λ_n refer to the eigenfunctions of the chamber and represented by $\lambda_{n}=(n+\frac{1}{2})\pi$, n=0,1,2,3,…….∞ and $C_{n}=\frac{2}{\lambda_{n}}\int_{x=0}^{x=1}-\varepsilon\omega\sin\lambda_{n}x dx$ and D_n=0. Once again assume the non-homogeneous solution for equation (20) is represented by u^(x, t) and retain the boundary conditions in (19)-(21) except $\frac{\partial u\,\hat{}}{\partial t}=0$ in (19). The general solution for the nonhomogeneous part of equation (19) for the non-resonance case is derived and written as;

$$u\,\hat{}\,(x,t)=\sum_{n=0}^{\infty}\left\{\begin{matrix}-2\dfrac{\varepsilon\omega^{3}}{\lambda_{n}^{2}\left(\lambda_{n}^{2}-\omega^{2}\right)}\sin\lambda_{n}t+\\ 2\dfrac{\varepsilon\omega^{2}}{\lambda_{n}\left(\lambda_{n}^{2}-\omega^{2}\right)}\sin\omega t\end{matrix}\right\}\sin\lambda_{n}x \quad (23)$$

Then the final non-resonance solution for the homogeneous and non-homogeneous wave equation that describe the acoustic velocity fields is derived from the summation of equations (22) and (23) ;

$$\tilde{u_{0}}(x,t)\Big|_{n\neq n^{*}}=\varepsilon\sin\omega t+\sum_{n=0,n\neq n^{*}}^{\infty}-2\frac{\varepsilon\omega}{\lambda_{n}^{2}}\sin\lambda_{n}t\sin\lambda_{n}x$$
$$+\sum_{n=0,n\neq n^{*}}^{\infty}\left\{\begin{matrix}-2\dfrac{\varepsilon\omega^{3}}{\lambda_{n}^{2}\left(\lambda_{n}^{2}-\omega^{2}\right)}\sin\lambda_{n}t+\\ 2\dfrac{\varepsilon\omega^{2}}{\lambda_{n}\left(\lambda_{n}^{2}-\omega^{2}\right)}\sin\omega t\end{matrix}\right\}\sin\lambda_{n}x \quad (24)$$

The resonance solution when $\omega=\lambda_{n}^{*}$ is derived from the non-homogeneous part by assuming the particular solution is proportional to the product of $t\cos\omega t$ and the final form is obtained and written as;

$$u_0^{\sim}(x,t)\Big|_{n=n^*} = \varepsilon \sin \omega t - \left(\begin{Bmatrix} \frac{1}{\lambda_n^*} \end{Bmatrix} \sin \lambda_n^* t + t \cos \lambda_n^* t \right) \sin \lambda_n^* x \quad (25)$$

Hegab [20] and Zhao et al. [13] described the irrotational acoustic system that employed by Flandro [14] and showed that the rest of the planer irrotational functions $\rho_0^{\sim}(x,t), T_0^{\sim}(x,t), and\ P_0^{\sim}(x,t)$ have mathematical relations to the velocity acoustic field $u_0^{\sim}(x,t)$ as follows;

$$\frac{\partial \rho_0^{\sim}}{\partial t} = -\frac{\partial u_0^{\sim}}{\partial x}, \frac{\partial u_0^{\sim}}{\partial t} = -\frac{1}{\gamma}\frac{\partial P_0^{\sim}}{\partial x}, \frac{\partial T_0^{\sim}}{\partial t} = \frac{\gamma - 1}{\gamma}\frac{\partial P_0^{\sim}}{\partial t} \quad (26)$$

In this study, the experimental measurement is constructed to record only the pressure acoustic fields at several locations along the chamber. For comparison considerations, the pressure equation can be derived from equations (24) and (26) with considering the pressure node (P=1) boundary conditions at the exit of the chamber. The final pressure equation for the nonresonance case is derived and written as;

$$P_0^{\sim}(x,t)\Big|_{n\neq n^*} = \gamma\varepsilon\omega \cos(\omega t)(x-1) + \sum_{n=0, n\neq n^*}^{\infty} \frac{2\gamma\varepsilon\omega}{\lambda_n^2 - \omega^2} \begin{pmatrix} \omega^2 \cos \omega t \\ -\lambda_n^2 \cos \lambda_n t \end{pmatrix} \cos \lambda_n x \quad (27)$$

Consequently, the final pressure equation for the resonance acoustic equation is derived as;

$$P_0^{\sim}(x,t)\Big|_{n=n^*} = \gamma\varepsilon\omega \cos(\omega t)(x-1) - \gamma\left(2 \cos \lambda_{n^*} t - \lambda_{n^*} t \sin \lambda_{n^*} t\right) \cos \lambda_{n^*} x \quad (28)$$

and the thermal acoustic field for the nonresonance and resonance solution is derived and written as follows;

$$T_0^{\sim}(x,t)\Big|_{n\neq n^*} = \frac{\gamma - 1}{\gamma} \left\{ \begin{matrix} \gamma\varepsilon\omega\cos(\omega t)(x-1) + \\ \sum_{n=0, n\neq n^*}^{\infty} \frac{2\gamma\varepsilon\omega}{\lambda_n^2 - \omega^2} \begin{pmatrix} \omega^2 \cos \omega t \\ -\lambda_n^2 \cos \lambda_n t \end{pmatrix} \cos \lambda_n x \end{matrix} \right\} \quad (29)$$

$$T_0^{\sim}(x,t)\Big|_{n=n^*} = (\gamma - 1) \left\{ \varepsilon\omega \cos(\omega t)(x-1) - \begin{pmatrix} 2 \cos \lambda_{n^*} t \\ -\lambda_{n^*} t \sin \lambda_{n^*} t \end{pmatrix} \cos \lambda_{n^*} x \right\} \quad (30)$$

and the perturbed density field is determined from;

$$\rho_0^{\sim}(x,t) = P_0^{\sim}(x,t) - T_0^{\sim}(x,t) \quad (31)$$

Equations (25)-(31) show the asymptotic analysis form for the time history of the perturbed flow variables $\left(P_0^{\sim}, T_0^{\sim}, \rho_0^{\sim}, and\ u_0^{\sim}\right)$ for the acoustic field

2.3 The Computational Approach

An accurate flow field time history in a SRM chamber can be obtained by using a finite difference scheme which shows the evolution of flow variables in the axial and transverse directions after many acoustic wave cycles. The present study employs higher order accuracy difference equations to minimize the impact of numerical diffusion found to affect results obtained from a second order explicit MacCormack code, Kirkkopru, et al. [24] Near the boundaries, the second order explicit predictor-corrector scheme, developed by MacCormack[25] is used to solve the 2-D, unsteady, compressible Navier-Stokes equations. At the interior points, the Navier-Stokes equations are solved numerically using the Two-Four explicit, predictor-corrector scheme, developed by Gottlieb et al.[26] which is a fourth-order variant of the fully explicit MacCormack scheme. This method, applied by Hegab, [20], Hegab, et.al. [21], and Kirkkopru et al.[24], is phase accurate and therefore suitable for describing many wave cycles and wave interaction problems. The grid points are equally spaced in each direction within the chamber. The number and spacing of the grid points used defines the accuracy and resolution of the local variations of flow variables in the axial and transverse directions.

Numerical solutions are obtained for several values of the parameter M, Re, n, and ω defined above. Generally δ=20 in order to describe flow dynamics in a long, relatively narrow chamber. The code has been run for several acoustic wave cycles to ensure that the solution converges to a steady state, defined by the condition that the total injected mass is equal to the total exiting mass and satisfies the condition:

$$\left(\phi_{i,j}^{t+1} - \phi_{i,j}^{t}\right) \approx O(10^{-k}) \quad (32)$$

where ϕ=(u,v,p,T) and k is an arbitrary coefficient based on the solution precision. Typical values of $k \leq 10^{-4}$. The computed steady state solution at given values of M, R_e, and δ, is then disturbed by an unsteady side-wall injection component added to the steady value. The total wall injection velocity for t > 0 is given by; $v_{rw}(x,1,t) = -1$.

The code has been run for many oscillation cycles in velocity and temperature to investigate the complete acoustic-fluid dynamic interactions across the chamber.

3. Experimental Set Up

The experimental set up layout is shown in Fig. 1. It consists of the following parts:

1-Electrical power supply
2-Cotrolled voltage circuit and constant voltage power supply device
3- AC motor
4- Pulley-belt system
5- Crank-shaft and piston mechanism
6- Geometry converter
7- Pressure transducer taps
8- To DAC
9-Distribution board
10- Voltage regulator
11 –Desktop computer

The piston oscillates at the head end of the tube. The acoustic pressure fields is recorded at several locations along the tube by capacitive pressure tranceducers (11). These tranceducers connected to a computer through built in data acquisition system (13)

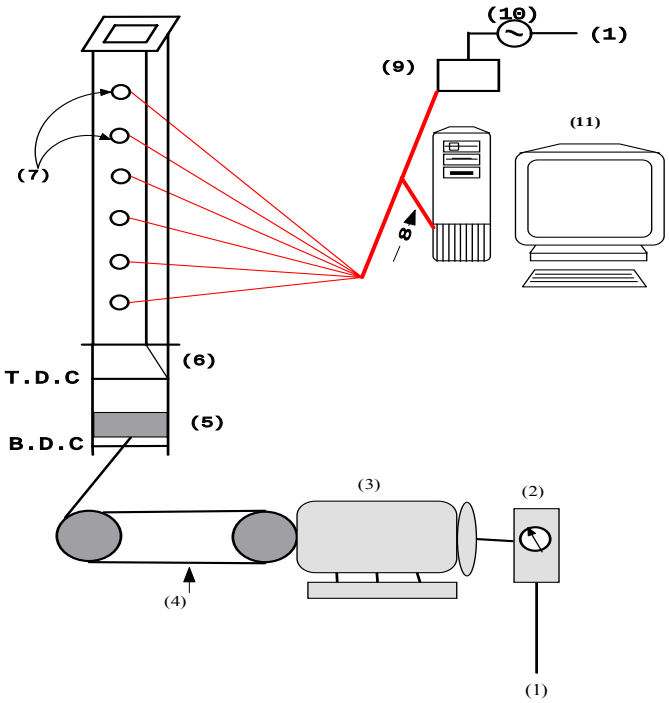

Figure(1): Layout of the Test Rig.

Results and Discussions

In this study the asymptotic methodologies is combined with the numerical and experimental approaches to give precise fundamental insights for the unsteady flow dynamics in a chamber with end wall disturbances and steady sidewall injection. The current results have been classified into two main categories. The first category of the results deals with the acoustic fields in the chamber without injection from the sidewall using the experimental, computational and analytical approaches. The experimental results are compared with the computational ones in order to validate the numerical technique. The last set of the results are from the computational approaches to study the generation and convection of vorticity and temperature flow dynamics due to the interaction between the acoustic disturbances that arises from the unsteady mass injection and the injected fluid.

The first set of the results show a comparison between the experimental pressure traces and the computational ones at x=0.125, ε=0.045, and ω = 0.52 (f = 63.44 Hz). The results illustrate the wave oscillations (quasi-steady wave motion) after many wave cycles. A stable or bounded solution is observed at this frequency. A reasonable comparison between the experimental and computational approaches is noticed. Further experimental results at different frequencies ω = 0.52, 0.54, and 0.65 are presented in figure (3). The motor frequencies is changed using voltage Variec. It is noticed that the range of the generated frequencies from the available devices is small enough to catch the first natural frequencies ω = π/2 (250 Hz). As a results the computational and asymptotic approaches are extended to cover a wide range of frequencies away from or very close to the first fundamental mode. A comparison of the asymptotic analysis pressure time history with the computational one is presented in figures (4) and (5) for ω=1 and 1.5, at ε=0.1. These results show good agreement between the analytical and computational solutions for $t < 20$, while the computational solutions show little damping to the higher harmonic as time increases. Generally both of the two approaches detect the coexistence of the forced mode and the system eigenfunctions oscillations for long period of running times. In addition, the co-existence of the forced and the eigenfunction modes for $t>>1$ is predicted in the earlier asymptotic analysis by Zhao, et al.[13], and Staab, et al.[11]. It is clearly noted that, the pressure and the axial velocity solutions are not purely harmonic for ω=1 (f=159 Hz). It is a combination of the forced mode oscillations and the eigenfunction waves. In contrast, the computational results by Kirkkopru, et al. [24] show *only pure harmonic oscillations*, represent the forced mode contributions without any consideration for the eigenfunctions modes. The reason behind these deficiencies may be probably related to the numerical boundary condition treatment which does not deal properly with the wave reflection at boundaries. As the frequencies increases beat phenomenon is appeared for both pressure and velocity fields.

The second set of the results is for unsteady velocity fields that is generated from the coexisting of the acoustic fields and the rotational velocity flow dynamics. The first case of the second set is implemented for the rotational velocity and vorticity when t= 32 for $Re = 3*10^5$, M=0.02, ε=0.4, at x=0.5 for ω=1 (dotted line), ω=1.5 (solid) in Fig. 6. The results imply that the unsteady vorticity field is generated at the side-wall and is then convected out toward the axis as time increases. The amplitude of the vorticity oscillations near the injection surface is generally larger than that away from the wall for both the non-resonance (ω=1) and the near-resonance (ω=1.5) frequencies. Moreover, the amplitudes of the rotational axial velocity and the vorticity for ω=1.5 is found to be about ten times than that for ω=1. While, The vorticity fronts for ω=1.5 and ω=1 observed approximately at the same transverse

locations. This interesting results reveal that the forcing frequency and the first fundamental modes have a great effect on the generation and evolution of the intense unsteady vorticity. The effect of the injected Mach number on the generation and evolution of the unsteady vorticity is presented in Fig. 7 at t= 32 for ω=1, Re= $3*10^5$, ε=0.4, at x=0.5 for M=0.02 (dotted line), M=0.01 (solid). It is noticed that the amplitudes of the axial rotational velocity and the generated unsteady vorticity increases as the injected Mach number increases. Moreover, the vorticity front for M=0.01 is located at y= 0.64, while for M=0.02 is found to be at y=0.4 from the centerline. This means that the vorticity field for the larger Mach numbers proceeds and fills faster than that the smaller Mach numbers. This trend is predicted by the analytically derived formula for the actual radial position as function of the Mach number and time as in Zhao et al [13],

$$\Omega_e(t) = \frac{2}{\sqrt{\pi}}\left(\tan^{-1}\left(e^{-M\pi t}\right)\right)^{1/2} \qquad (33)$$

This derived front location is measured from the centerline. Figure (8) shows the analytical time dependent vorticity front location (Ω_e) at different Mach numbers varies from 0.01-0.04. A comparison between the asymptotic analysis equation (33) and the computational solution for the front locations at time t=32 at Mach number M=0.01 and 0.02 show an excellent qualitative and quantitative agreements.

The transverse variations of rotational axial velocity and the vorticity at several different times at the med length of the chamber for Re = $3*10^5$, M=0.02, ε=0.4, and ω=1 is presented in figure (9). The results imply that the unsteady vorticity field is generated at the side-wall and is then convected out toward the centerline as time increases. The rotational field extends to cover nearly the entire chamber by t =42, where the effect of the interaction between the generated acoustic waves and the injected fluid at the surface is prolonged.

The unsteady vorticity topography at two different times t=20 and 40 for Re =$3*10^5$, M=0.02, δ=20, and ε=0.4 is presented in figure (10). At x=[0,1] represent the closed and open ends of the chamber, while at y=[0,1] represent the centerline and the injection surface respectively. At the sidewall y=1, T=1 is specified. It is noted that the absolute amplitude of the unsteady vorticity increases with increasing axial distance downstream. Moreover the vorticity front moves almost parallel to the injection surface and the monotonic variation is noticed. This trend is predicted by the analytically derived formula for the wall vorticity $\Omega_w(x,t)$ in Staab et al. [11], where the local amplitude of vorticity is found from the ratio of the local acoustic pressure gradient to the local instantaneous injection rate. The axial derivative $\partial\left|\Omega_w(x,t)\right|/\partial x > 0$ implying that the magnitude of vorticity generated on the wall increases downstream. Since the vorticity is convected into the chamber by the transverse flow field, one may expect relatively larger values of the vorticity near the injection surface at large axial locations. At the exit, the magnitude of the vorticity close to the injection surface is as large as 20, suggesting that the scaling O(1/M) found in the asymptotic analyses, Staab et al. [11] and Zhao et al.[13] is appropriate.

The last case study of the second set is for the generation and evolution of the temperature disturbance that accompany the vorticity generation in the first case study. Fig. (11) show the transverse temperature variations at the med length of the chamber for Re =$3*10^5$, M=0.02, δ=20, and ε=0.4 at five different times. It is clearly noted that, the fluctuation of the transverse temperature gradient at the injection surface found to be about larger than that away from the injection surface. Here again the variation can be attributed to a combination of oscillations at the forcing frequency and eigenfunction oscillations that exist for t>>1. Near the centerline the temperature represent the values for the pure acoustic fields that studied in details in the first set of the study.

Conclusions

Computational, analytical, and experimental approaches have been employed to study the dynamic process in a simulated solid rocket motor chamber with the goal of understanding the vorticity and temperature dynamics caused by significant steady sidewall mass addition along with end wall disturbances. The temperature and the vorticity field generated in a low Mach number and a large Reynolds number flow have described.

Results for the acoustic field show a bounded solution for the non-resonance frequency, while beats phenomena is observed near-resonance frequency. A reasonable comparison between the experimental and computational approaches is noticed. Generally, the computational and analytical approaches detect the coexistence of the forced mode and the system eigenfunctions oscillations for long period of running times. In addition, the co-existence of the forced and the eigenfunction modes for t>>1 is predicted in the earlier asymptotic analysis by Zhao et al.[13], and Staab et al.[11]. It is clearly noted that, the pressure and the axial velocity solutions are not purely harmonic for ω=1 (f=159 Hz). It is a combination of the forced mode oscillations and the eigenfunction waves. In contrast, the computational results by Kirkkopru et al. [24] show *only pure harmonic oscillations*, represent the forced mode contributions without any consideration for the eigenfunctions modes. The reason behind these deficiencies may be probably related to the numerical boundary condition treatment which does not deal properly with the wave reflection at boundaries. As the frequencies increases beat phenomenon is appeared for both pressure and velocity fields.

The computational results for the rotational fields that is generated from the interaction between the steady side wall injection and the acoustics show that, after the end wall disturbances is initiated, the acoustic disturbances interact with the injected fluid to generate a large amplitude of vorticity and temperature at the side-wall. For appropriate ranges of Reynolds number, Mach number, and frequency, the vorticty

and temperature waves are transported into the chamber by the transverse velocity component of the flow field.

The amplitude and the wavelength of the spatial oscillations near the injection surface is generally larger than that away from the wall. In the context of propellant combustion, one may anticipate that the intensive unsteady vorticity generation will persist to the surface of a burning solid propellant in a real rocket chamber and are likely to impact the characteristics of the combustion process.

In general, results of the kind described here may help to identify high heat transfer and erosional burning location in SRM chambers. An understanding of oscillatory, intense axial shear stress and heat transfer on the side-wall will be useful for developing physically viable boundary conditions at the decomposing interface of a burning solid propellant. The interesting idea here has a great reflect on our model for the burning of microstructure solid rocket motor propellant combustion.

NOMENCLATURE

$C_{p_o}^{'}$	Specific heat at constant pressure
E_T	Total energy
$H^{'}$	Chamber-half height
$L^{'}$	Length of planar chamber geometry
M	Mach number
$P_o^{'}$	Exit pressure from the chamber
P_r	Prandtl number
$r_b(x,t)$	Combustion products from solid propellant.
R_e	Flow Reynolds number
R_{e_A}	Acoustic Reynolds number
SRM	Solid Rocket Motor
$T_o^{'}$	Temperature of the injected fluid
$t_a^{'}$.	Time is non-dimensionalized with respect to the axial acoustic time
$U_{zo}^{'}$	An axial flow characterized. $U_{zo}^{'} = \delta V_{yo}^{'}$
u,υ	Dimensionless Velocity components in x,y directions.
$V^{'}_{yo}$	Velocity of inert gas which injected through the porous side walls

Greek symbol

$v'_{rws}(x)$	The *steady* injection velocity component
ε	Amplitude of the generated acoustic wave.
$\delta^{'}$	Aspect ratio ($L^{'}/H^{'}$)
ρ	Density
γ	Specific weight
$\mu_b^{'}$	Dynamic viscosity
$k_b^{'}$	Conductivity coefficient

The superscripts

(o)	Refer to characteristics flow variables
(')	Refer to the dimensional quantities.
($_{os}$)	Refer to the computed steady state flow
(^)	Represent the flow variable perturbation

REFERENCES

1. Erickson R., Markopoulos N., and Zinn, B. "Finite Amplitude Acoustic Waves in Variable Area Ducts" AIAA-01-1099, 39th AIAA Aerospace Sciences Meeting and Exhibit, , 8-11 January 2001, Reno, NV, USA.
2. Zaripov, R.G. and. Ilhamov, M. A 'Nonlinear Gas Oscillations in a Pipe' J. Sound vol.., 46, pp 245-257, (1976)
3. Merkli, P. and Thomann, H. " Thermoacoustic Effects in a Resonance Tube" J. Fluid Mech., V.70, pp.161-177, July 1975
4. Meng Wang and Kassoy, D.R. " Nonlinear Oscillation in a Resonant Gas Column: An Initial-Boundary Value Study" SIAM J. Appl. Math., V.55, No. 4, pp. 923-951, August 1995
5. Jimenez, J. ' Nonlinear Gas Oscillation in Pipes. Part1. Theory' J. Fluid Mech.(1973), Vol. 59, part 1, pp.23-46
6. Ahmed A. Sileem" Nonlinear Evolution of Resonant Acoustic Oscillations in a Tube Ended With Variable Area Portion" International Conference on Energy Research & Development (ICERD, Nov., 9-11-1998), Kuwait.
7. Ahmed A. Sileem and M. Nasr, "An Experimental Study on Finite Amplitude Oscillations in Ducts: The Effect of Adding Variable Area Part to The Open End of Constant-Area Resonant Tube", Alexandria Engineering Journal, Faculty of Engineering Alexandria University, EGYPT, pp 397- 409, Vol 42, No. 4, January 2003.
8. Brian R. Seymour and Michael P. Mortell ' Resonant Acoustic Oscillation with Damping: Small Rate Theory' J. Fluid Mech.(1973), Vol. 58, part 2, pp.353-373
9. J.H.M. Disselhorst and L. Van Wijngaarden 'Flow in the Exit of Open Pipes during Acoustic Resonance' J. Fluid Mech. (1980), vol. 99, part 2, pp. 293-319.
10. Garcia-schafer, J. E. and A. Linan. "Longitudinal acoustic instabilities in slender solid propellant rockets: Linear analysis" J. Fluid Mech. (2001), vol. 437, pp.229-254
11. Staab, P.L., Zhao, Q., Kassoy, D.R., Kirkkopru, (**1999**), "Co-existing Acosutic- Rotational Flow in a Cylinder with Axisymmetric Sidewall Mass Addition", Physics of Fluids, **11**, 10, 2935-2951.
12. Rempe M., Staab, P.L., and Kassoy, D.R. (**2000**), "Thermal Response for an Internal Flow in a Cylinder with Time-Dependent Sidewall mass Addition", AIAA 2000-0996, 38th Aerospace Science Meeting, Reno, NV.

13. Zhao, Q., Staab, P.L., Kassoy, D.R., and Kirkkopru, K. (**2000**), "Acoustically Generated Vorticity in an Internal Flow," J. Fluid Mech., #**13**, 247-285.
14. Flandro, (1995), " Effect of Vorticity on Rocket Combustion Stability" Journal of Propulsion and Power, Vol. **11**, 607-625.
15. Majdalani and W. Van Moorhen (**1998**), "Improved Time-Dependent Flow Field Solution for Solid Rocket Motors", AIAA Journal, **36**, 241-248.
16. Vuillot, F., and Avalon, G. (1991), " Acoustic Boundary Layers in Solid propellant Rocket Motors Using Navier-Stokes Equations," J. Propulsion and Power, **7**, No.1 231-239.
17. Smith, T.M., Roach, R.L., and Flandro, G.A. (1993), "Numerical Study of the Unsteady Flow in a Simulated Solid Rocket Motor," AIAA Paper, 93-0112, 31th Aerospace Science Meeting, Reno, NV.
18. Tseng, C.F., and Tseng. I.S.,(1994), "Interaction Between Acoustic Waves and Premixed Flames in Porous Chamber," AIAA 94-3328, 32th Aerospace Science Meeting, Reno, NV.
19. Roh, T.S., and Yang, V. (1995), "Transient Combustion Responses of Solid Propellants to Acoustic Disturbances in Rocket Motors," AIAA Paper, 95-0602, 33th Aerospace Science Meeting, Reno, NV.
20. Hegab, A.M. (**1998**) "A Study of Acoustic Phenomena in Solid Rocket Engines", Ph.D. Thesis, Mech. Power Engineering Dept., Menoufia Univ., Egypt, (Carried out at the University of Colorado at Boulder).
21. Hegab, A.M., Kassoy, D.R., and Sileem, A.A. (**1998**), "Numerical Investigation of Acoustic-Fluid Dynamics Interaction in an SRM Chamber/Nozzle Model" AIAA Paper 98-0712, 36th Aerospace Science Meeting ,Reno, NV.
22. Vetel, J., Plourde, F., Kim, S. D., and Guery, J.-F., "Numerical Simulations of Wall and Shear Layer Instabilities in A Cold Flow Set-Up", J. of Propulsion and Power, Vol. 19, No. 2, 2003, PP. 297-306.
23. Vetel, J., Plourde, F., and Kim, S. D. " Amplification of a Shear-layer Instability by Vorticity Generation at an Injecting Wall", AIAA Journal, Vol. 42, No. 1, 2004, PP. 35-46.
24. Kirkkopru, K., Kassoy, D.R., and Zhao, Q. (1996), " Unsteady Vorticity Generation and Evaluation in a Model of Solid Rocket Motor," J. of Propulsion and Power, **12**, No. 4, 646-654.
25. MacCormack, R.W. (1982), " A Numerical Method for Solving the Equations of Compressible Viscous Flow," AIAA J., **20**, No. 9, 1275-1281.
26. Gottlieb, D., and Turkel, E. (1976) "Dissipative Two-Four Methods for Time-Dependent problems," Mathematics of Computation, **30**, No. 136, 703-723.

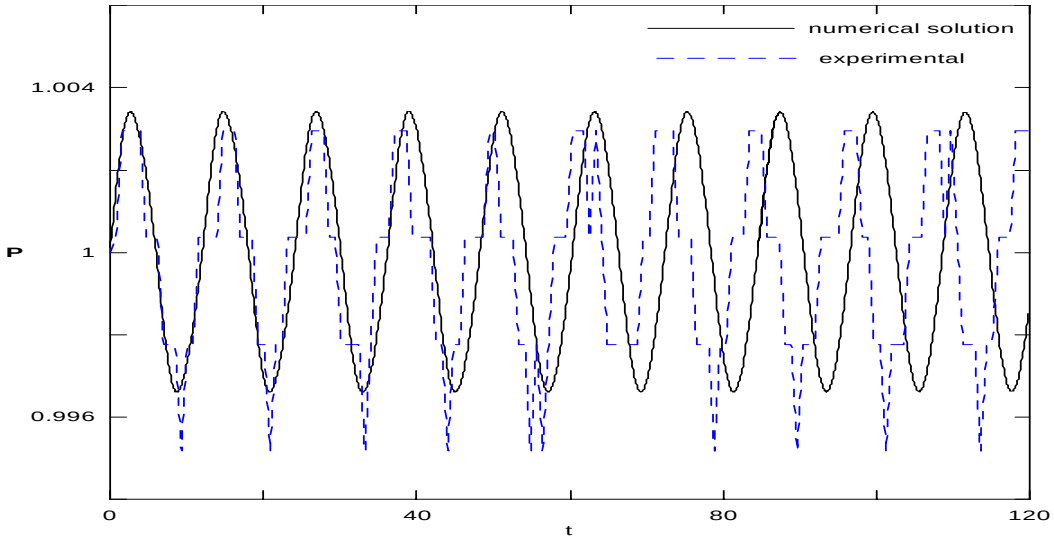

Figure(2): Comparison between the experimental and computational results for the pressure time history at x=0.125, ε=0.045, ω = 0.52 (f = 63.44 Hz).

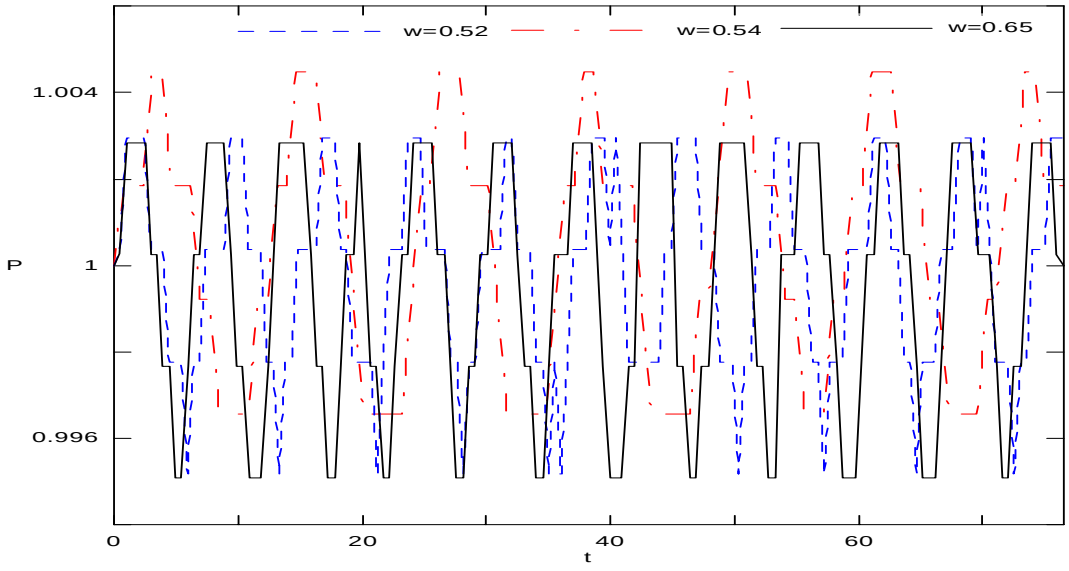

Figure(3): The pressure time history recorded at several forcing frequencies ω = 0.52, 0.54, and 0.65 at x=0.125

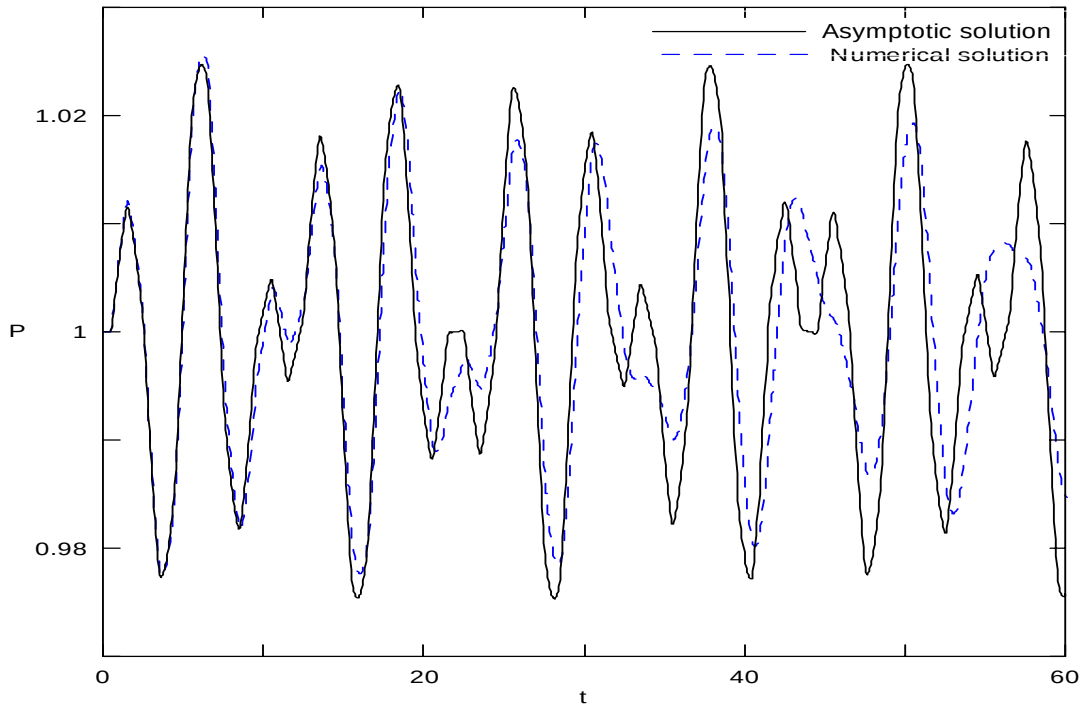

Figure(4): Comparison between the computational and analytical results for the pressure time history at the med length of the chamber, ε= 0.1 , ω = 1.0 (f`=159 Hz).

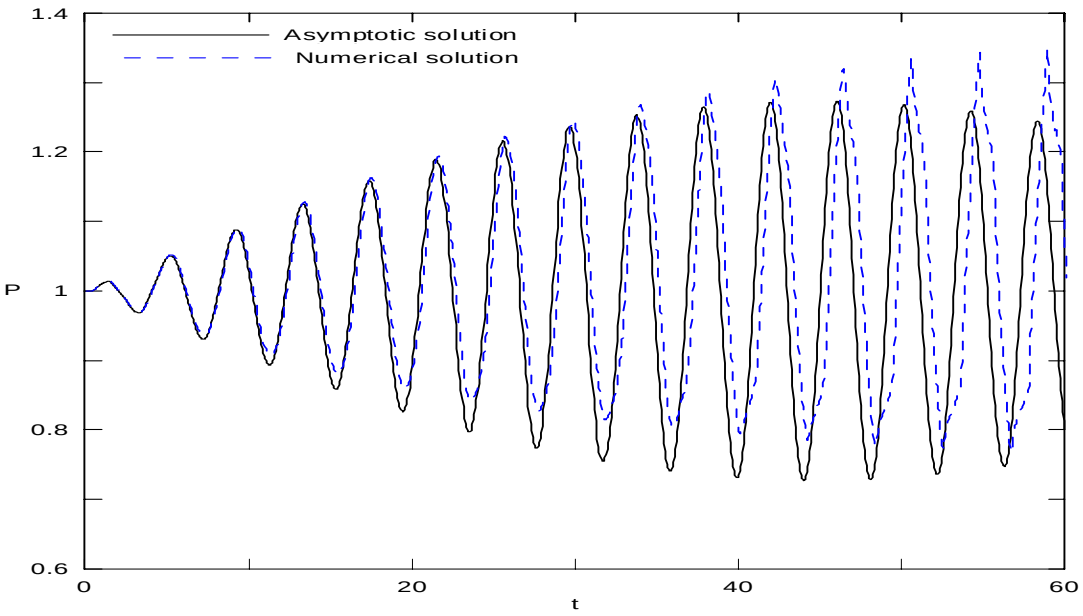

Figure(5): Comparison between the computational and analytical results for the pressure time history at the med length of the chamber, ε= 0.1, ω = 1.5 (f`=239 Hz).

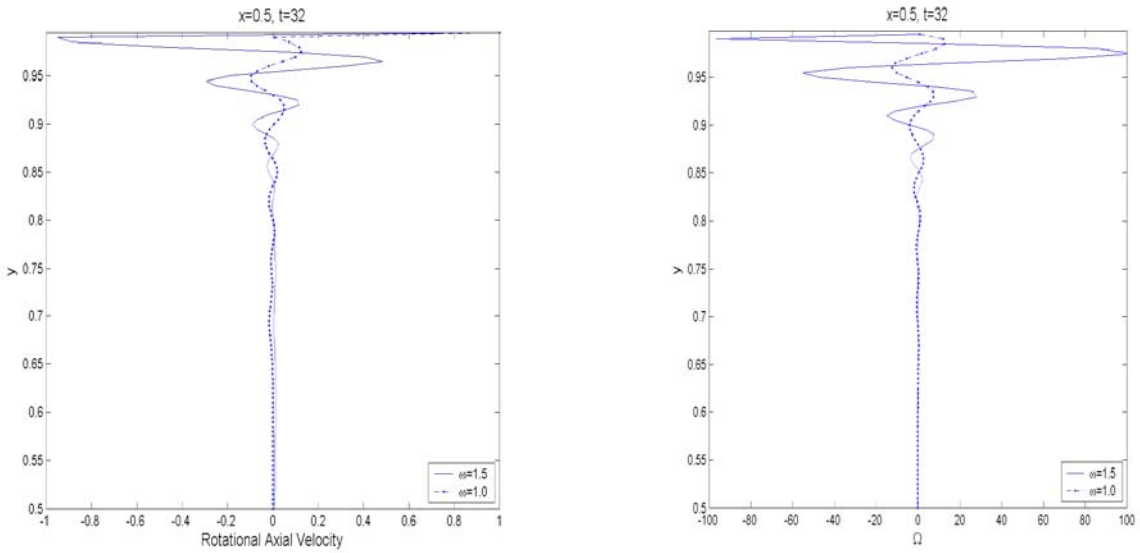

(a) (b)

Figure (6): Computational results for the transverse variations of (a)Rotational axial velocity (b)Unsteady vorticity across the chamber at x=0.5 and t=32 for ω=1 (dotted), ω=1.5 (solid).

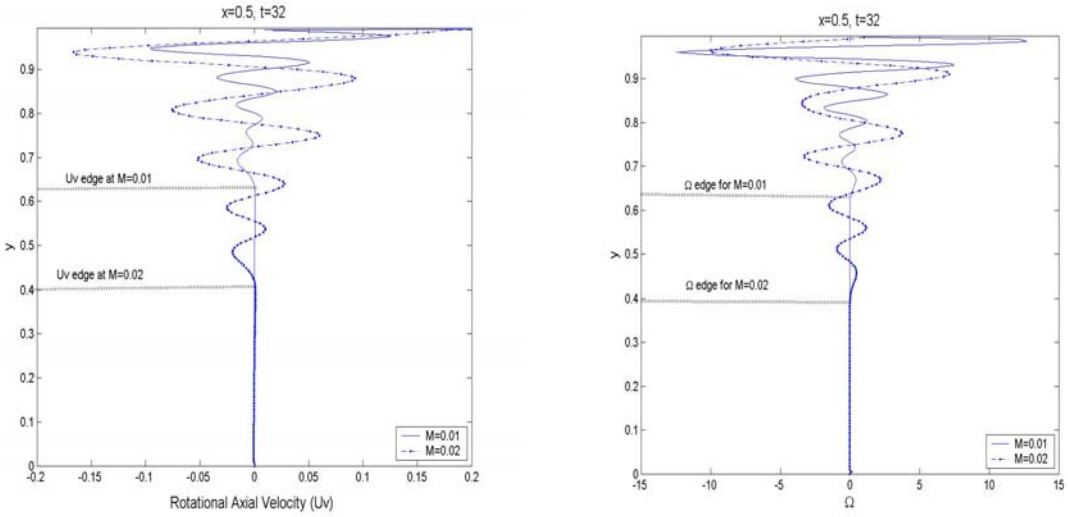

(a) (b)

Figure (7) : Computational results for the transverse variations of (a) Rotational axial velocity (b) Unsteady vorticity across the chamber at x=0.5, t=32, and ω=1 for M=0.02 (dotted line), M=0.01 (solid).

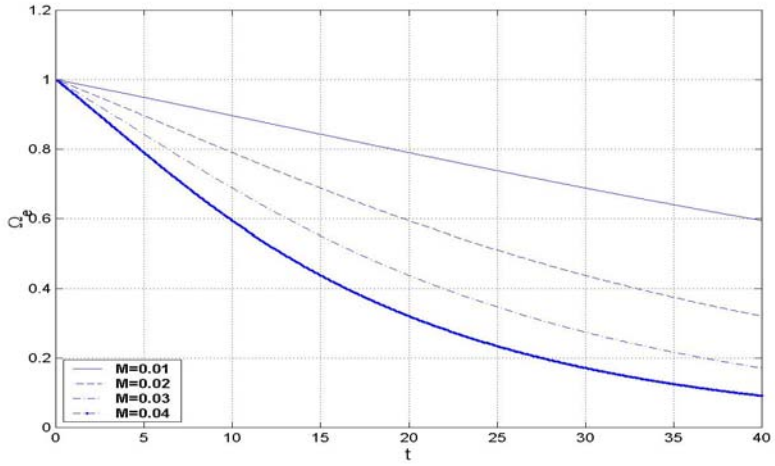

Figure (8) : Analytical time dependent vorticity front location (Ω_e) at different Mach numbers.

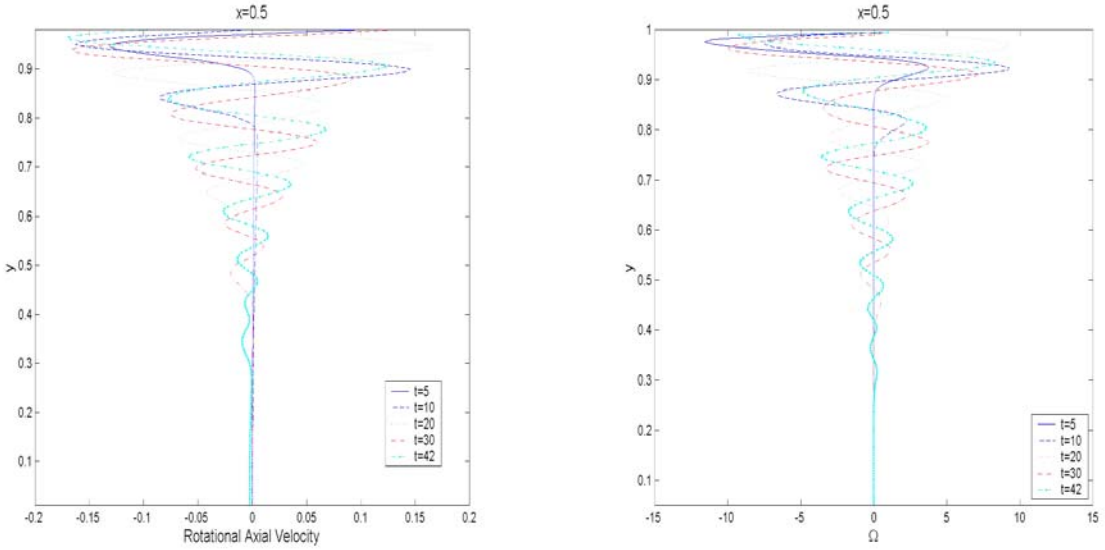

Figure (9): Computational results for the transverse variations of (a) Rotational axial velocity (b) Unsteady vorticity across the chamber at x=0.5, ω=1 for M=0.02 at five different times.

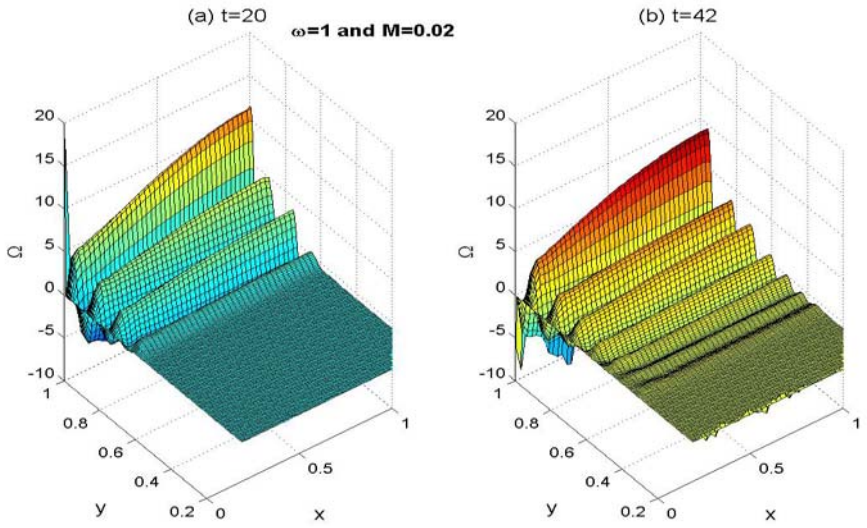

Figure (10): Computational results for the vorticity topography at $Re=3*10^5$, M=0.02, δ=20, and ε=0 and t= 20, 42.

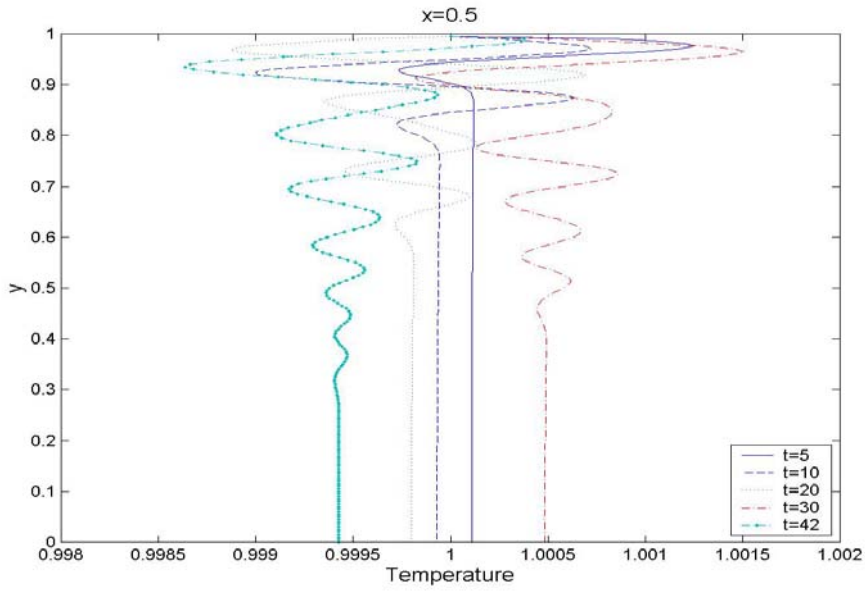

Figure (11): Computational results for the transverse variations of the temperature across the chamber at x=0.5, ω=1 for M=0.02 at five different times.